An experimental investigation of high aspect-ratio rectangular sails

By A. Crook, M. Gerritsen † AND N. N. Mansour

1. Problem statement and relevance of proposed research

The flow around a sail is sensitive to external conditions such as the boat heel, boat speed and atmospheric conditions. The flow may also be Reynolds-number dependent, with typical Reynolds numbers in the range of 1-10 million. Aeroelastic effects of the sail can be important especially in downwind sailing. The performance of the sail is highly dependent on the sail trim. Designing a sail is in many senses more complex than an aircraft wing of high aspect ratio where the ambient conditions are known and are less dynamic. A Velocity Prediction Program (VPP) is used to take into account the performance of the yacht when designing a sail. The VPP solves a set of equations that govern the motion of the yacht. However modelling the aerodynamics of the yacht remains a large problem: see Jackson (1996). Sail performance characteristics usually come from CFD for upwind sails, whereas for downwind sails wind tunnel tests are the preferred method due to the high computational cost of downwind CFD simulations.

At present, VPPs use semi-empirical data to calculate the forces on the hull and sails. An experimental database of sail properties and characteristics would allow the validation of Computational Fluid Dynamics (CFD) codes and their implementation in the VPP.

The fluid dynamics of sails is also poorly understood, although the previous experiments discussed in this brief provide a base from which our knowledge can be further enhanced. The foremost reason for investigating two-dimensional sails is that the flow around three-dimensional sails is highly dependent upon the sail geometry and sailing conditions. For upwind sailing, the sail performance is highly sensitive to sail trim. A three-dimensional model sail is very difficult to trim, and the trim required would change with the varying flow angles and boat heel and direction. A three-dimensional sail experiment also requires that the freestream flow direction change with increasing distance from the foot of the sail. This is necessary to simulate the change in effective wind angle that the sail experiences as it travels through the Earth's atmospheric boundary layer.

Team New Zealand have made use of a twisted-flow tunnel at The University of Auckland in New Zealand (Flay (1996)) for downwind testing of 1/10 scale three-dimensional sail-hull configurations, and this has proved to be very useful in refining existing designs. The flow is twisted using a set of turning vanes, but the twist has to be changed for any change in the boat's speed or heading. For the reasons mentioned, upwind testing of the sail is infeasible.

An experimental investigation of two-dimensional, high-aspect-ratio sails using sail sections representative of that used on modern yachts will therefore provide a generic database that will have a large impact on the sailing industry in terms of providing a database for CFD validation and also enhancing the sail designer's physical understanding of the complex fluid dynamics.

† Stanford Yacht Research, Stanford University

1.1. *Sail flow characteristics and the current state of the art*

The current state of the art in sail design is different for upwind and downwind sails. For the upwind conditions the camber of the sail and the angle of incidence of the apparent wind to the sail are small, resulting in largely attached flow. A leading-edge separation bubble may be present, especially in the presence of a mast. Wind tunnel testing by racing teams is rare due to the problem of trimming at model scale. Upwind sail performance is highly sensitive to trim because of the small angles of incidence involved, meaning that small changes affect the performance significantly. Upwind sail flow analysis is generally performed using panel methods, and sometimes Euler codes. The design starts as a series of two-dimensional sections that vary with the height of the sail, and that are then blended together to form a three-dimensional sail. The three-dimensional sail is then optimized further by coupling 3D panel methods, some of which can implement twisted onset flow, to a finite-element structural-analysis program to try to predict the flying shape.

Physical understanding of the flow around generic sail sections at representative Reynolds numbers is limited. An enhanced understanding of the flow physics around sail sections is required as a first step to understanding the more complex flow around a three-dimensional upwind sail.

Three-dimensional upwind sails may have separated flow at the head of the sail whilst the flow remains attached elsewhere as a result of the twisted onset flow. This greatly influences the sail design and trim. To reduce separation near the head, the sail is usually twisted also. Generally, strong tip vortices are shed off the head and the foot of the sail. As a result, the induced drag is large, and may contribute as much as 15% of the total boat drag (including hull, rigging and wave drag). Heeling of the boat also significantly affects the performance of the sails. It is also important to understand the sensitivity of the two-dimensional flow to Reynolds number, wind direction, camber and the effects of the mast and its orientation with respect to the sail. Such parameters will affect the transition behaviour of the flow, the size of the leading edge separation bubble if any, and the location of the trailing-edge separation. A correlation of these flow features with the corresponding sail pressure distribution, lift and drag will be invaluable in understanding how to better design sails to provide the greatest amount of forward thrust without exceeding a given rolling moment (Wood and Tan (1978)).

In reaching (i.e. partial-downwind conditions), the angle of incidence is larger. The flow on the main sail and gennaker or spinnaker is complex due to the presence of large scale separation for higher incident wind angles. If the flow is separated at the leading edge it is important to know how large the bubble is and also for what conditions the flow reattaches. At higher angles of incidence, the flow is likely to be unsteady. This unsteady behaviour affects the dynamic behaviour of the sail. Flow simulation requires the use of viscous solvers and turbulence models. Because of their expense and limited expertise in the sailing industry, wind tunnel testing is the preferred method of testing. However, the same limitations of many upwind experiments such as low aspect ratio and purely force and moment data are also seen for the downwind experiments. For the downwind case, it is therefore important to provide flow topology and force/pressure data on sails with realistic camber and high aspect ratio for a range of wind angles and Reynolds numbers.

There have been two seminal series of experiments that have attempted to address some of the fundamental questions regarding 2D sail flows, with and without masts, carried out by Milgram (1971), Milgram (1978) and Wilkinson (1984), Wilkinson (1989) and Wilkinson (1990).

Milgram (1971) investigated highly-cambered (camber ratio (defined as the ratio of

maximum camber to chord) greater than 10) thin airfoils (without masts) with the NACA 65 (Abbott and von Doenhoff (1959), p.386) and $a = 0.8$ (Abbott and von Doenhoff (1959), p.402) mean lines. The experiments were conducted in a water tunnel at three different Reynolds numbers of 6, 9 and 12×10^5. These high Reynolds numbers were achieved through the use of water as the working fluid and by the use of relatively large-chord sections. The relatively small dimensions of the water tunnel meant that the aspect ratio of the airfoils was low, being equal to approximately 2.2. For highly-cambered sections, a low aspect ratio may cause spanwise three-dimensionality in the separating flow, although this was not addressed in Milgram's report.

Data for the highly-cambered sections is in the form of lift, drag and pitching-moment coefficients for a range of angles of attack. The experimental setup uses dynamometers to measure the forces and moment, with one side of the airfoil clamped and the other side pinned. A consequence of this arrangement is that the airfoil twists under load, with two degrees of twist reported for angles of attack greater than ten degrees.

For the range of camber ratios investigated for the NACA 65 and $a = 0.8$ mean line , the aerodynamic characteristics are similar and do not vary greatly over the limited Reynolds number range in which the tests were conducted. A typical $C_L - \alpha$ plot shows a linear increase in C_L up to 4 degrees angle of incidence, followed by a small drop in C_L and then a recovery in C_L up to approximately 20 degrees. The maximum value of C_L increases with camber ratio for a given thickness distribution as one would expect and ranges between approximately 2 and 2.6. A typical plot of C_D versus C_L shows an almost linear decrease in C_D with C_L until a plateau is reached where C_D is a minimum (approximately 0.06) and fairly constant with C_L until the airfoil stalls and the drag rises sharply. With increasing camber ratio, the sharp increase in drag at the end of the plateau is preceeded by a reduction in C_L for increasing C_D. The size of this reversal increases with increasing camber. The pitching-moment coefficient, C_m, defined at the quarter-chord point, is always negative because the center of pressure is significantly aft of the quarter-chord point, and becomes more negative with increasing camber ratio. The slope of the $C_m - \alpha$ through zero angle of incidence is negative, followed by a minimum at around 4 degrees, and then a positive slope before another change in slope just before stall.

These characteristics are different from those of conventional, airfoils with low camber and moderate thickness, the data for which can be found in Abbott and von Doenhoff (1959). Thin airfoil theory predicts pre-stall lift versus angle of incidence fairly well for these sections. For highly cambered, thin sections, the C_L is always less than predicted, with the slope of the curve greater than 2π/radian for angles of attack less than the theoretical ideal angle of incidence (defined as the angle of incidence at which the forward stagnation point just lies on the leading edge). The slope is less than 2π/radian for angles of attack greater than the ideal angle of incidence (figure 1).

Milgram (1978) tested one mean line (NACA $a = 0.8$) for two different camber ratios (0.12 and 0.15) with circular and elliptic-shaped masts of different diameters. The data are again limited to lift and drag coefficients, although the longitudinal location of the center of pressure is included as a function of C_L. The tests were carried out in the same water tunnel as used Milgram (1971), but without the turbulence screens, which resulted in measured values of C_D for the sections without a mast being 10% higher than in the earlier tests.

The addition of a circular mast with a diameter to chord ratio (d/c) of 0.15, does not significantly change the C_D-C_L behaviour for CR=0.15, and extends the C_L range

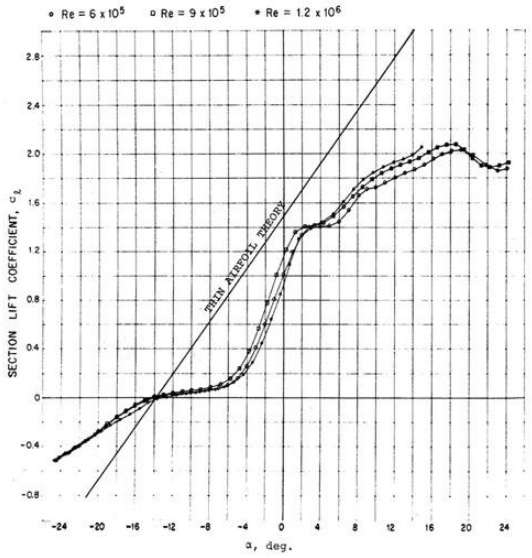

FIGURE 1. Comparison of C_L versus α for NACA 65 mean line with CR=0.12 as predicted by thin airfoil theory and measured experimentally (Milgram (1971)).

of the CR=0.12 section before the onset of the sharp drag rise. The difference in C_D between the two different camber ratio sections is a slowly increasing function of C_L for the circular mast (d/c=0.15). However the addition of an elliptic mast (d/c=0.17, where d in this case is the square root of the mast cross-section area), causes the C_D-C_L curve to be shifted to the right for the lower camber ratio meaning that the CR=0.12 section has a lower C_D over the whole range in C_L and the difference in C_D between the two increases rapidly with increasing C_L.

The behaviour of C_D versus C_L is a smooth function of d/c over the Reynolds number range investigated ($0.5 - 1.5 \times 10^6$), except for the two largest diameter elliptical masts tested (d/c=0.31 and 0.36). For these two masts, C_L/C_D is much larger than would be expected by extrapolating the data from lower values of d/c. This indicates that the large masts are causing a different flow structure to occur with larger regions of separation. The use of trip devices on the elliptical mast with d/c=0.31 partly confirms this idea because the drag is reduced with their addition, presumably because of a delayed separation from the mast. For d/c=0.36, the effects of adding the trip devices upon the C_D-C_L plot are opposite for the two different Reynolds numbers tested. The data is largely insensitive to Reynolds number over the range examined, except for the d/c=0.36 elliptical mast without trip devices.

Milgram concludes that a common range of mast-sail geometries for a broader range of camber ratio still need to be investigated. Also since the value of d/c is typically large near the head of sails, further study of sections at high C_L for large values of d/c is required. The addition of a mast to the sail raises the friction and form drag to the same order of magnitude as the induced drag of the sail, whereas without the mast the friction and form drag would be small by comparison.

Wilkinson (1984) took Milgram's experiments with the mast attached one step further, and measured pressure distributions and velocity profiles for NACA $a = 0.8$ and 63 mean lines with a circular mast attached. Tests with the NACA 63 mean line investigated the

effect of moving the point of maximum camber forward. Wilkinson conducted the tests in the $7' \times 5'$ tunnel at Southampton University, England at Reynolds up to 1.6×10^6. As with Milgram's tests, a low-aspect-ratio sail was tested to achieve high Reynolds numbers, and therefore three-dimensional flow at high angles of attack cannot be ruled out. Unfortunately neither of the series of experiments report surface-flow visualisation which is an easy tool in determining the large-scale flow structure.

The experiment set out to look at the effects of sail camber distribution, camber ratio, Reynolds number, angle of incidence, mast diameter/chord ratio and mast angle. In total of 216 tests were carried out, and it was concluded that all the pressure distributions could be represented by one universal form of pressure distribution that could be divided into nine regions as shown in figure 2.

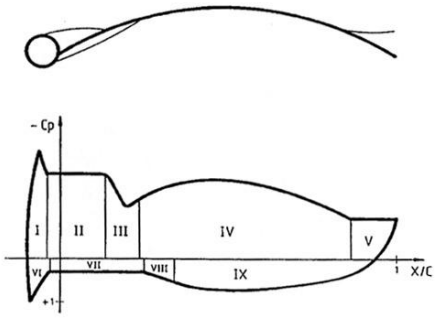

REGION	DESCRIPTION
I	Upper Mast Attached Flow Region
II	Upper Separation Bubble
III	Upper Reattachment Region
IV	Upper Aerofoil Attached Flow Region
V	Trailing Edge Separation Region
VI	Lower Mast Attached Flow Region
VII	Lower Separation Bubble
VIII	Lower Reattachment Region
IX	Lower Aerofoil Attached Flow Region

FIGURE 2. Universal pressure distribution: see Wilkinson (1984)

Over the limited Reynolds-number range investigated, little effect was observed. Increasing angle of incidence tended to decrease the base pressure in the upper-surface separation bubble and to shorten the length of the bubble. The pressure distribution also flattened out on the upper surface (region IV), and the position of the trailing-edge separation moved upstream. Increasing d/c has the effect of increasing the size of the separation bubble, flattening out the pressure distribution in region IV and reducing the extent of the trailing-edge separation. Finally, the effect of the two sail shapes tested on the aerodynamic characteristics appears to be small. The pressure recovery at reattachment is larger for the NACA 63, the minimum pressure in region IV occurs further forward, and on the lower surface the pressure distribution is much fuller.

From the review of Milgram and Wilkinson's work, it is obvious that the sections and even the masts tested may not be representative of real sails and masts. Furthermore, the data gained in both series of experiments provided a foundation for understanding

more about sail flows but is limited because three-dimensional flow effects may be large due to the low aspect ratio of the airfoils tested. With modern testing techniques the understanding gained from these seminal experiments can be built upon, further enhancing our understanding of this most complex flow.

2. Research aims and objectives

In summary, the primary aims of this experimental study are to:

• Gain a deeper physical understanding of the flow past upwind and downwind sails under various angles of incidence and Reynolds numbers.

• Create a comprehensive database for validation of numerical solvers and turbulence models that can be used by the (sail) research community and industry at large.

The objectives to achieve these aims for a range of two-dimensional sail sections and apparent wind angles are:

• For select upwind and downwind sections use Particle Image Velocimetry (PIV) to understand the effect of Reynolds number upon the flow topology, which may include the size and structure of leading-edge separation bubbles with and without a mast for the upwind case, location of trailing-edge separation if present, and the structure and frequency of the wake (measured using a hot wire or Laser Doppler Velocimeter (LDV)). Furthermore, the sensitivity of the pressure distribution and sectional lift and drag coefficients (C_L and C_D, respectively) to Reynolds number will be addressed using Pressure Sensitive Paint (PSP) and a wake rake of total-pressure tubes.

• For all six sail sections use a range of tools including surface oil-flow visualization, PSP, oil-film interferometry and/or shear-sensitive liquid crystals, to understand the main flow topology on both surfaces such as mean separation locations and transition location if no leading-edge separation is present.

• To measure sectional lift and drag coefficients, and the skin-friction distribution for all six sail sections, with and without a mast for the upwind cases, and to correlate this with the flow topology.

• For a select upwind case, to investigate in detail the interaction between the mast and sail for a range of sail incidences and effective wind angles with respect to the mast. PIV will be used to measure the flow structure and PSP and the wake rake to measure the section lift coefficient and drag coefficient, respectively.

3. Technical approach

We propose an initial test of six sail and mast configurations, to be conducted in February-June 2003 in the NASA Ames $7' \times 10'$ tunnel. The configurations are listed in table 1 and shown in figures 4-7. All models will be cambered plates of high aspect ratio, with constant cross section. Initial CFD studies have shown that the aspect ratio must be chosen as 15 or higher to sufficiently reduce three-dimensional effects. Measurements will be taken near mid-span. Alternatively, tangential blowing can be used with wings of lower aspect ratio to achieve higher Reynolds numbers. This option will be investigated.

The thin steel models will be put under tension to reduce the risk of buckling in the tunnel, and will be formed to the desired shape using matching machined blocks place in compression. The structural package MSC.Nastran will be used to aid the model design, with pressure loads predicted using the CFD package CFX. The sail shape will be formed

	Sail Type	Model	$7' \times 10'$ tunnel	$12'$ tunnel
Upwind	Genoa (mid-mast height)	Supplied by TNZ	*	
	Mainsail (mid-mast height)	Supplied by TNZ	*	*
	With and without mast		*	
Downwind	Dynarig (Maltese Falcon)	Circular arc 12.5% camber	*	
	Genneker	Circular arc 20% camber	*	
	Genneker (TNZ)	Circular arc 25% camber	*	*

TABLE 1. List of sail configurations to be tested

by using thin steel, with two clamping blocks, machined to the desired profile, at each end as shown in figure 3. Appropriate boundary conditions will be applied in Nastran to simulate deforming the steel sheet. The predicted pressure distribution will then be applied to determine the thickness of the steel sheet and the amount of spanwise tension required in order to maintain the sail shape across the span. A small-scale model of the tensioning mechanism with a scaled high-aspect ratio thin steel sail will be constructed to prove the concept. Even with tensioning it is expected that the sail will deflect under aerodynamic load. The flying shape of the sail will therefore be measured using photogrammetric techniques available at NASA Ames. Vibration of the sail sections may also be an issue, particularly for cases where large regions of separated flow exist.

It is planned to test each section shape over a range of angles of incidence, and to determine the sectional pressure and skin friction distribution for each, from which the lift and drag coefficient can be found. In addition the structure of the flow away from the surface will be investigated, with particular emphasis on the regions of separation near the leading and trailing edges.

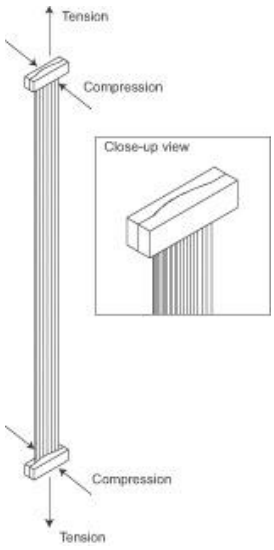

FIGURE 3. High-aspect-ratio 2D sail shape formed by shaped clamps placed under spanwise tension

3.1. *Sail geometries*

3.1.1. *Upwind Sails*

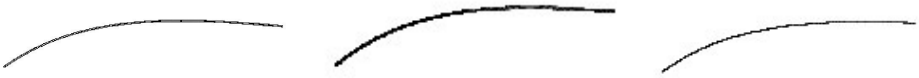

(a) Mainsail mid-height (b) Mainsail $\frac{3}{4}$ height (c) Genoa mid-height

FIGURE 4. Upwind sails. Source: Team New Zealand. All sections shown at 18 degrees apparent wind angle

3.1.2. *Reaching and downwind sails*

The America's Cup gennaker cross-sections are close to circular arcs with 20-25% camber. We will test 20% and 25% camber. The Dynarig sections are circular arcs with 12.5% camber.

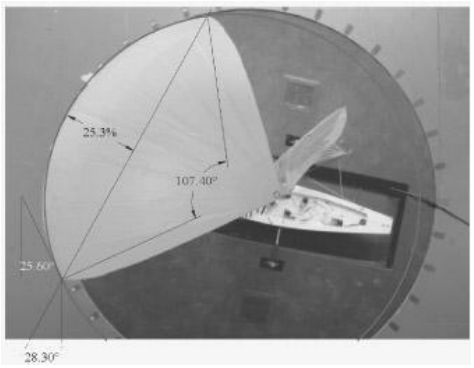

FIGURE 5. Typical TNZ gennaker - 25.3% circular arc. Picture taken in wind tunnel at Auckland

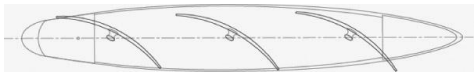

FIGURE 6. Dynarig sail configuration - 12.5% circular arc

3.1.3. *Masts*

Source: Team New Zealand. Dimensions full-scale (near head) are 200mm × 150mm.

(a) (b)

FIGURE 7. Masts for upwind tests: (a) Cut-off ellipse, (b) Cut-off ellipse, rounded edges. Source: Team New Zealand

3.2. *Experimental facilities and techniques*

All models will be tested in the $7' \times 10'$ closed-return wind tunnel at NASA Ames. This wind tunnel is capable of a maximum freestream speed of 200 knots (103 m/s) and has a freestream turbulence intensity of approximately 0.25%.The tunnel will be run at a speed of 30-40 m/s, leading to a chord Reynolds number of approximately half a million. This velocity is low enough to avoid compressibility effects, but high enough to utilize techniques such as PSP which need a reasonable dynamic pressure to work well. The closed-return tunnel also simplifies the process of seeding the tunnel for optical techniques such as PIV and LDV. After the experiments are performed, two designs (one upwind, one downwind) will be tested in the $12'$ pressurized tunnel at NASA Ames at higher Reynolds numbers, to conduct Reynolds-number sensitivity analyses. Using this tunnel Reynolds numbers of up to 4 million per foot (6 atm pressure) can be achieved at a Mach number of 0.1. Designing a thin sail to withstand such high dynamic pressures will not be an easy task, and performing the tests at a lower pressure of 2 atm (Reynolds number of 1.4 million per foot at Mach 0.1) is more feasible.

3.2.1. *Pressure Sensitive Paint (PSP)*

PSP will be used on the upper and lower surface of the sail to determine the pressure distribution around the section, and also by integrating the pressure distribution, to calculate the section lift coefficient. PSP is applied to a highly-reflective surface and luminesces when excited molecules in the coating return to a lower energy state due to the collision with an oxygen molecule in a process known as oxygen quenching. Excitation is commonly provided by a UV lamp. The rate of quenching is proportional to the partial pressure of oxygen, which is in turn proportional to the air pressure. PSP is therefore most sensitive to changes in pressure when the dynamic pressure is high and the percentage change in pressure is high with respect to atmospheric pressure. A typical setup for PSP is shown in figure 8.

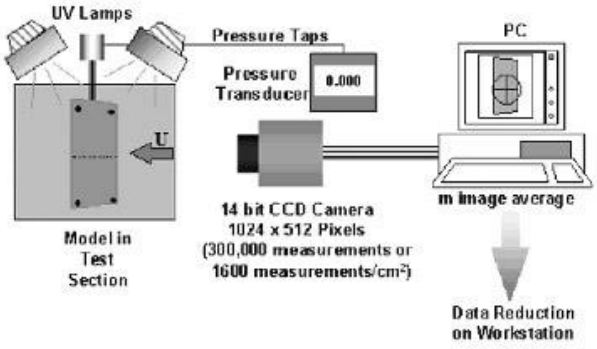

FIGURE 8. A typical PSP setup: from Bell *et al.* (2001)

The ratio of wind-on to wind-off intensity of the emitted light from the PSP is proportional to the ratio of respective pressures under conditions of constant excitation. The constants in the governing equation are derived either before the experiment by measuring the intensity of the PSP for various pressures and temperatures and/or during the experiment by using a reference pressure on the model such as that provided by a pressure transducer. Photogrammetry may then be required to associate the points in the PSP image with those on the model.

Uncertainty in the measurement of pressure can be due to errors in the calibration of the response of the paint to pressure, spatial and temporal variations in illumination and errors in the data processing. By far the largest source of error comes from the uncertainty in the paint's temperature.

Sullivan (2001) states that the accuracy of PSP is 1 mbar with a resolution of 0.5 mbar, and that the typical time response is 0.5 seconds, although 1 μs has been demonstrated. For further information on PSP, the reader is referred to Bell *et al.* (2001), Mehta *et al.* (2000) and Sullivan (2001).

Illustrations of the ability of PSP to capture the pressure distribution with high resolution over a large area and range of pressure are given in figures 11a and 11b.

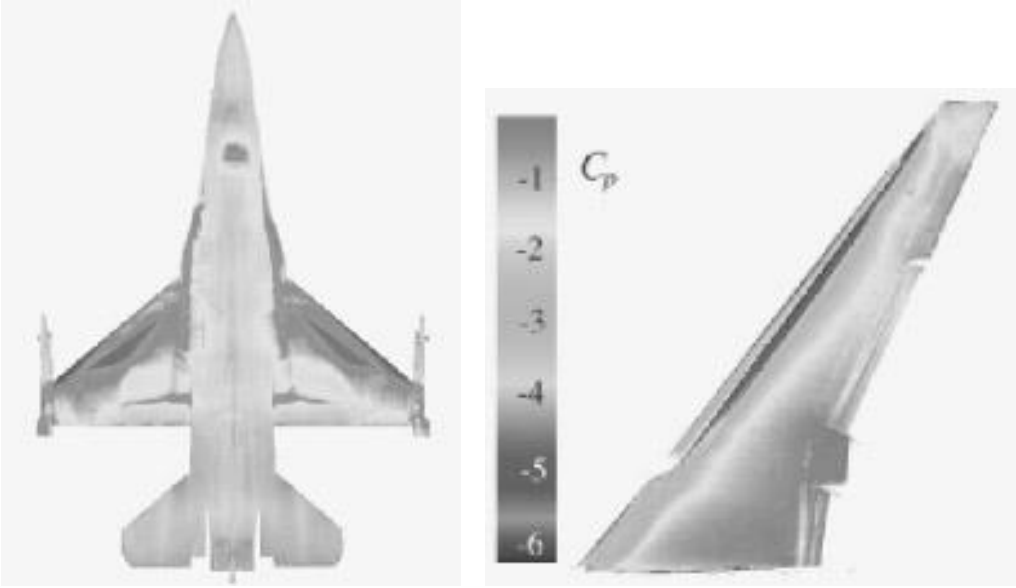

(a) Upper surface of an F-16 (b) High-lift wing

FIGURE 9. Pressure distributions measured using PSP (Bell *et al.* (2001))

3.2.2. *Oil-film interferometry*

Oil-film interferometry relies on the principle that the rate at which oil thins on a surface is a function of the shear-stress magnitude. There are various incarnations of oil-film interferometry as discussed by Naughton and Sheplak (2000), although the method used at NASA Ames is Fringe Imaging Skin Friction Interferometry (FISF). The interference between the partially-reflected light at the air-oil interface and the light reflected from the model surface will vary between constructive and destructive as the oil film thickness changes. This is observed as a series of light and dark bands or fringes, the spacing of which is proportional to the skin friction (Figure 10).

The oil typically used is silicone oil and is applied to the surface in either square patches or drops. The surface should have a high index of refraction (ideally $n = 2$), and therefore glass is ideal. For practical reasons, polished stainless steel or Mylar is often used. The light absorption of aluminium is too low to be used with PSP.

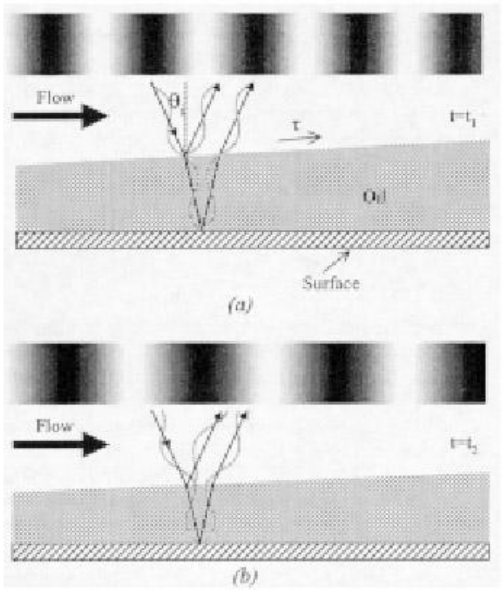

FIGURE 10. Interference fringes produced by Fizeau Interferometry: (a) Constructive interference produces bright bands, whereas (b) destructive interference produces dark bands (Naughton and Sheplak (2000))

Illumination must be provided by a coherent light source, although the coherence length can be short (a few microns) due to the small thickness of the oil film. Light sources such as fluorescent bulbs, sodium lamps and black lights are often used. Lasers suffer from the expense of special optics and also the problem of specular reflection (speckle) near the surface. Imaging can be achieved using CCD cameras, preferably black and white. Calibration of the oil viscosity and its variation with temperature is necessary, although the measurement of the shear stress is absolute, requiring no additional reference measure. Mehta *et al.* (2000) state that using calibrated oil and with an accurate measurement of the dynamic head and the incident light angle, it is possible to achieve accuracy in the skin friction coefficient, c_f, better than $\pm 5\%$ in magnitude and $\pm 1\%$ in vector direction.

Examples of oil film interferometry applied to wing flows are given in figures 13a and 13b. In figure 13a, oil drops are applied to a wing tip and provide both the magnitude and direction of the surface shear stress. In figure 13b oil patches are applied to a transport wing to yield the magnitude of surface shear stresses.

3.2.3. *Particle Image Velocimetry (PIV)*

Modern PIV calculates the velocity field in a plane by comparing two images containing particles separated by a very short time interval. The flow field of interest is usually illuminated by a thin laser sheet at these two times, with each laser pulse triggering the capture of the particle field using a cross-correlation CCD camera that is placed normal to the plane of the laser sheet (Figure 12). This type of CCD camera is capable of capturing two images in very quick succession (usually 10 μs apart). A cross-correlation algorithm is then used to locate intensity peaks in both images for small areas (of the order of 64×64 pixels) and this is repeated across the whole image. The peak in the correlation should correspond to the same particle in both images. The distance each particle moves in terms

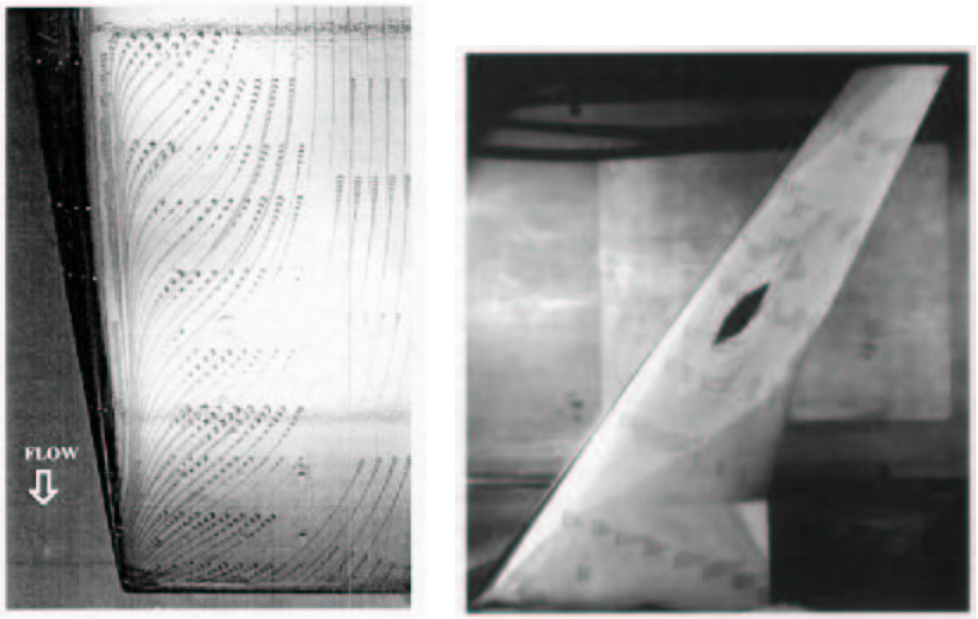

(a) Oil-drop method applied to a wing tip (Naughton and Sheplak (2000))

(b) Oil patches applied to a transport aircraft wing (Mehta *et al.* (2000))

FIGURE 11. Examples of oil film interferometry applied to aircraft wings

of pixels (and physical space via a calibration) in the time separating the two images can then be calculated, yielding the instantaneous velocity vector in the plane. From this data other properties of the flow, such as vorticity, can be calculated (Figure 13), and if sufficient frames are captured, flow statistics such as the rms and mean velocity components and therefore stresses, skewness and kurtosis can be calculated. Extension of the technique to measuring the out-of-plane velocity component, and therefore the full velocity vector, is possible by utilising perspective error. If the CCD camera is placed at 90 degrees to the laser sheet, the angle of view at the edges of the image will decrease from the optimal 90 degrees at the center of the image, and the motion of particles perpendicular to the laser sheet can be detected. Stereoscopic or 3D PIV requires two cross-correlation CCD cameras placed at approximately 40 degrees to the laser sheet. This obviously causes a problem with focus as different parts of the laser sheet are at different distances from the camera lens. This can be overcome by using a large depth of field which results in a small lens aperture and low light intensity at the CCD. The Scheimpflug condition for focusing solves this problem. It states that if the image plane if the CCD sensor and the lens plane are coincident at the focus plane of the lens, then the particles in the laser sheet will be in focus on the CCD sensor.

The temporal resolution of PIV is governed by the repetition rate of the laser and the CCD camera. In general these are usually 15–30 Hz, although high speed PIV at frequencies up to 1 MHz is possible using cinematic cameras and high frequency lasers and multiple CCD cameras. Spatial resolution is also limited by the CCD element and

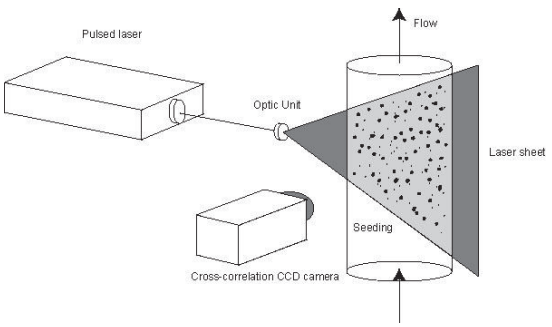

FIGURE 12. Typical 2D PIV setup

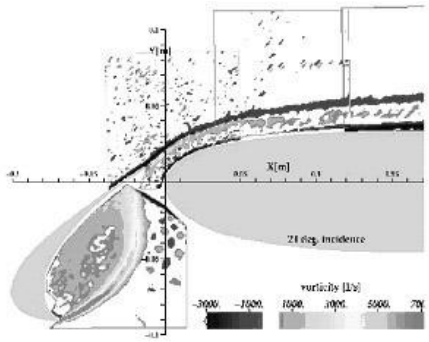

FIGURE 13. Mean spanwise vorticity measured using PIV for a high-lift system (Stanislas *et al.* (2000))

the number of pixels and their size. An example of a high-end CCD camera is one with 1280×1024 pixels and a pixel length of 6.7 μm.

For more information on PIV, the reader is referred to Gharib and Daribi (2000), Grant (1994) and Adrian (1991).

We will determine the pressure distribution, the size of leading-edge bubbles, the trailing-edge separation points and the skin friction in all tests. The pressure distribution will be measured using Pressure Sensitive Paint (PSP). Skin friction will be measured using oil-film interferometry or shear-sensitive liquid crystals. Particle Image Velocimetry (PIV) will be performed on two upwind and two downwind designs to create a detailed picture of the flow past the sail and in the wake. Expertise in all of the measurement techniques described is available at NASA Ames and Stanford.

We will return to the $7' \times 10'$ wind tunnel in late 2003 to test sail shapes for the Maltese Falcon suggested by our optimization algorithm (Doyle *et al.* 2002).

REFERENCES

ABBOTT, I. H. & VON DOENHOFF, A. E. 1959 *Theory of wing sections. Including a summary of airfoil data.* Dover, New York.

ADRIAN, R. J. 1991 Particle–imaging techniques for experimental fluid mechanics. *Annu. Rev. Fluid Mech.* **22**, 261–304.

BELL, J. H., SCHAIRER, E. T., HAND, L. A. & MEHTA, R. D. 2001 Surface pressure measurements using luminescent coatings. *Annu. Rev. Fluid Mech.* **33**, 155–206.

DOYLE, T., GERRITSEN, M. & IACCARINO, G. 2002 Towards sail shape optimization of a modern clipper ship. *Annual Research Briefs,* Center for Turbulence Research, NASA Ames/Stanford Univ.

FLAY, R. G. J. 1996 A twisted flow wind tunnel for testing yacht sails. *J. Wind Engng and Indust. Aerod.* **63**, 171–182.

GHARIB, M. AND DARIBI, D. 2000 Digital Particle Image Velocimetry. In: *Flow Visualization: Techniques and Examples.* (A. J. Smits and T. T. Lim, eds.), Imperial College Press, London.

GRANT, I. (ED). 1994 *Selected papers on particle image velocimetry.* SPIE Milestone Series MS 99.

Jackson, P. S. 1996 Modelling the aerodynamics of upwind sails. *J. Wind Engng and Indust. Aerod.* **63**, 17–34.

Mehta, R. D., Bell, J. H., Reda, D. C., Wilder, M. C., Zilliac, G. G. & Driver, D.M. 2000 Pressure and sensitive coatings. In: *Flow Visualization: Techniques and Examples* (A. J. Smits and T. T. Lim, eds.), Imperial College Press, London.

Milgram, J. H. 1971 *Section data for thin highly cambered airfoils in incompressible flow. NASA* CR-1767, 1971.

Milgram, J. H. 1978 Effects of masts on aerodynamics of sail sections. *Marine Tech.* **15**, 35–42.

Naugthon, J. W. and Sheplak, M. 2001 Modern skin friction measurement techniques: Description, use and what to do with the data. *AIAA Paper* 2000–2521.

Stanislas, M., Kompenhans, J. & Westerweel, J. 2000 *Particle Image Velocimetry: Progress towards Industrial Application.* Kluwer, Dordrecht.

Sullivan, J. 2001 Temperature and pressure sensitive paint. In: *Advanced Measurement Techniques,* (Sleverding, C.H., ed.) Lecture Series 2001–01, von Karman Institute for Fluid Mechanics.

Wilkinson, S. 1984 Partially separated flows around 2D masts and sails. Ph.D. thesis, University of Southampton.

Wilkinson, S. 1989 Static pressure distributions over 2D mast/sail geometries. *Marine Tech.*, **26**, 333–337.

Wilkinson, S. 1990 Boundary–layer explorations over a two–dimensional mast/sail geometry. *Marine Technology*, **27**, 250–256.

Wood, C. J. & Tan, S. H. 1978 Towards an optimum yacht sail. *J. Fluid Mech.* **85**, 459–477.